POLITECNICO DI TORINO
Repository ISTITUZIONALE

Investigation of a GDI injector with an innovative flowmeter for high-pressure transient flows

Terms of use:

(Article begins on next page)

15 May 2024

1   **Investigation of a GDI injector with an innovative flowmeter for high-pressure transient flows**

2   Alessandro Ferrari[1], Pietro Pizzo[2] and Oscar Vento[1,*]

3   [1] Energy Department, Politecnico di Torino, Corso Duca degli Abruzzi 24, 10129, Torino, Italy

4   [2] Rabotti Srl, Via Gino Capponi 13, 10148, Torino, Italy

5   * Corresponding author. E-mail address: oscar.vento@polito.it

6   **Abstract**

7   A new flowmeter for high pressure flows, characterized by intense dynamic events, is presented. The

8   flowmeter algorithm is based on the measurement of two pressure signals along the investigated pipe, and the

9   flowrate is obtained through an ordinary differential equation that is obtained from the combination of the

10   continuity and the momentum partial differential equations. This flowmeter has been applied to a GDI injector

11   to monitor the flowrate that enters the injector during an injection event. A 1D numerical model of the GDI

12   injector has been set up and validated, and the numerical outcomes have been used to confirm the consistency

13   of the experimental results obtained from the new flowmeter, for both single and pilot-main injections. The

14   internal dynamics of the injector has also been investigated, using both the 1D numerical tool and the

15   innovative flowmeter. A possible feedback-control strategy has been set up to compensate for any inaccuracy

16   of the injected mass by applying the flowmeter to the hydraulic high-pressure circuit.

17   **Keywords**

18   GDI injector; instantaneous flowrate measurement; high-pressure flow; innovative flowmeter; closed-loop

19   control.

20   **1. Introduction**

21   The prediction of an instantaneous high-pressure flowrate in fluid power hydraulic circuits can only be

22   obtained by developing numerical models in which all the main hydraulic, mechanical, and electromagnetic

23   characteristics are taken into account. However, an extensive validation against experimental transients is

24   required to guarantee an adequate accuracy of these models [1]. Such an approach suffers from the absence of

25   a flowmeter featuring the following characteristics: reduced dimensions and non-invasiveness, an excellent

26   dynamic response, and the ability to work under high-pressure levels.

Various technologies and operating principles have been developed for flowrate measurements. Turbine flowmeters are used to measure the frequency generated by the rotation of a rotor, which is directly proportional to the flowrate [2]. These steadily calibrated devices can be applied to measure unsteady flowrates [3], but only pulsating [4], [5] or intermittent [6] ones with a lower frequency than 1 kHz can be considered.

Orifice flowmeters are widely diffused in industry, due to their simplicity in terms of construction and installation [7], [8]; however, they are generally employed for steady-state flows [9] and particular correction curves have to be employed to modify the steady equation for pulsating flows [10].

Electromagnetic flowmeters are suitable for flows characterized by a pronounced frequency content, but the constraint on the required electrical conductivity of the measured fluid, which should be lower than 0.1 uS/cm, excludes the possibility of applying this category of flowmeters to diesel or gasoline engines, since both are characterized by a much lower conductivity than that of the aforementioned threshold [11].

The currently available Coriolis flowmeters can be applied for the measurement of a flowrate characterized by a pressure of up to around 400 bar [12], although modern diesel injection systems can reach pressure levels of up to 3000 bar [13], while the 500 bar level is the target for next-generation GDI systems [14]. However, the invasiveness of this family of devices may represent a limit to their application [15].

In this context, a flowrate estimation, based on the measurement of instantaneous pressure traces, represents a very attractive opportunity, due to the characteristics of the pressure sensors, in terms of miniaturization and dynamic response [16]. If the layout of the hydraulic system ensures that the pressure wave propagation occurs along a single direction, a mathematical relation between the measured pressure time history and that of the flowrate can be established for each pipe section [17]. However, if the pressure waves travel back and forth along the pipe, as in the rail-to-injector pipe of a Common Rail system [18], one pressure signal is not enough for the evaluation of the time distribution a consistent flowrate.

In the present investigation, an instantaneous high-pressure flowrate has been determined by measuring two pressure traces through the use of piezoresistive transducers. A first-order nonlinear ordinary differential equation has been obtained by combining Euler's mass conservation and momentum balance equations, where both the steady-state and the unsteady friction terms have been considered. The presented flowmeter, which has already been satisfactorily applied to Common Rail systems [19] (with pressures of up to 1800 bar) and to

, to investigate its internal fluid dynamics . Furthermore, a possible closed-loop control strategy of the injected mass, which is based on the application of the presented flowmeter to the fuel injection hydraulic circuit, is presented.

2. Experimental facilities

Tests were performed in the research laboratory at the Rabotti headquarter. The hydraulic test bench is a Rabotti TEC201 Evolution. It is composed of a conventional fuel injection system test stand featuring an electric motor, the speed of which can be controlled over the 0-4000 rpm range, a thermal regulation system of the tank and a low-pressure feeding circuit, which allows the high-pressure pump to be filled with pressurized oil over the 0-40 bar range. A typical Common Rail module is installed on this bench. This module contains the high-pressure pump, the rail, and some measurement devices (pressure and temperature sensors, Coriolis flowmeter, Injection Analyzer). The driving signals to the injector and to the rail/pump pressure control devices, i.e. the pressure control valve (PCV) and the fuel metering valve (FMV), are generated by an in-house developed control unit that offers the possibility of freely managing the injection pressure, the number of injections, the energizing time of each shot (ET), the dwell time between each shot (DT), the injection frequency and the configuration of the injector current profile (voltage, current levels and duration of each phase of the driving command).
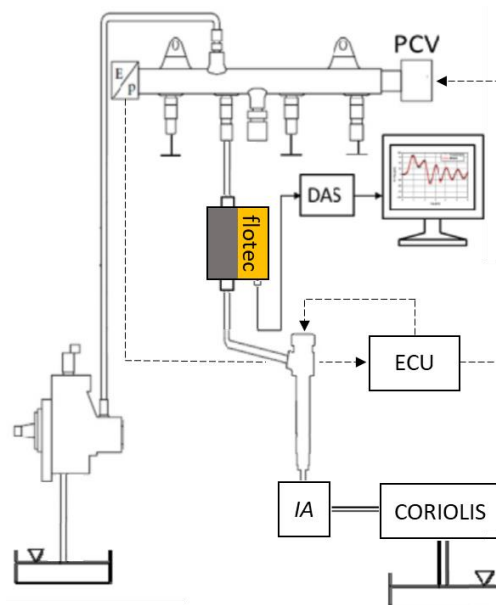

Fig. 1 – Layout of the experimental apparatus.

73 Furthermore, it can be used in either manual mode, by introducing the test operative conditions and recording

74 the test results manually, or automatically, using a pre-recorded test plan.

75 A scheme of the experimental layout is shown in Fig. 1. A high-pressure rotary pump feeds the rail to which

76 the injector is connected, through an 840 mm long pipe, with an internal diameter, d, of 2 mm. This pipe is

77 equipped with the new high-pressure flowmeter, which has been called "Flotec". The flowmeter, represented

78 as a colored box in Fig. 1 and in the photos in Fig. 2, is constituted by a piece of pipe onto which two

79 piezoresistive pressure sensors are mounted at a distance l=200 mm from each other. The upstream pressure

80 sensor, p_{up}, is 320 mm far from the rail, while the pressure sensors p_{dw} is 200 mm far from p_{up} (and closer to

81 the injector). This portion of pipe is installed between the rail and the tested injector, as shown in Fig. 2a,

82 where the two pressure sensors constituting the flowmeter can be seen, while, in Fig. 2b, the flowmeter is

83 presented with its external shell.
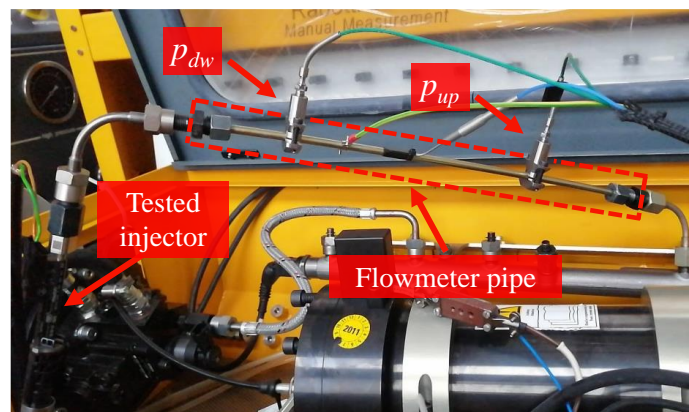
84
85 *(a) The flowmeter pipe equipped with the two pressure sensors.*

86
87 *(b) The flowmeter with its external shell.*

88 *Fig. 2 - Pictures of the Flotec flowmeter installed in the GDI injection system.*

89

90   The employed piezoresistive transducers present an accuracy of ±1.25 bar. Because of the difficulty of

91   measuring the flow temperature (in order to evaluate the flow properties, such as density and dynamic

92   viscosity), a thermocouple (accuracy ±2 °C), which is directly linked to the fluid temperature, is used to

93   measure the temperature of the external surface of the pipe between the two pressure sensors, and the flow

94   temperature is thus obtained with a simple sub-model. The portion of the pipe in which the thermocouple is

95   placed has been insulated in order to quickly reach a steady-state measurement, as the operative condition of

96   the system is modified. The injected flowrate is measured by the Injection Analyzer, that is, a Bosch method-

97   based flowmeter (labelled "*IA*" in Fig. 1, with an accuracy of $<\pm 0.1$ mg/shot), in which the pressure signal is

98   measured downstream of the injector tip and the injected fuel travels along a 11 m long pipe to prevent pressure

99   wave reflections that could disturb the ongoing injection event; a Coriolis flowmeter, placed downstream of

100   this pipe, measures the average flowrate ($\leq \pm 0.1\%$ accuracy of the measured flowrate).

101   The GDI injector, a scheme of which is shown in Fig. 3, is normally closed, because the spring preload and

102   the fuel pressure create a closure force. When the current signal acts on the injector, a magnetic force, generated

103   at the solenoid, pushes the needle up until it reaches its stroke-end (the injector is not ballistic), thus making

104   the injection start. As soon as the current signal is switched off, the magnetic force becomes null, the needle

105   reaches the end of its downstroke and the nozzle closes, and this determines the end of the injection. Because

106   of the absence of a pilot stage, the GDI injector can be assimilated to a fast two-way electro-valve with an inlet

107   and one outlet port.
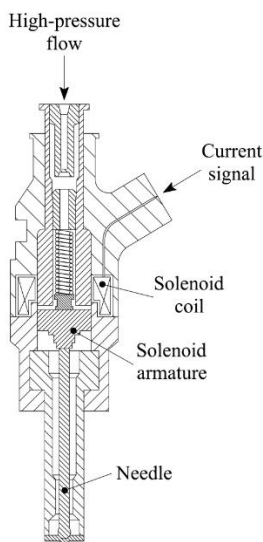
108

109   *Fig. 3 – Scheme of the GDI Injector.*

3. Flowmeter algorithm

The one-dimensional form of the partial differential equations of the continuity and momentum balance of a slender pipe can be written as [22]:

$$
\begin{cases}
\dfrac{d\rho}{dt} + \rho \dfrac{\partial u}{\partial x} = 0 \\[2ex]
\dfrac{\partial u}{\partial t} + u \dfrac{\partial u}{\partial x} + \dfrac{1}{\rho}\dfrac{\partial p}{\partial x} = -\dfrac{4\tau_w}{\rho d}
\end{cases}
\tag{1}
$$

where u, p, and ρ indicate the fluid velocity, fluid pressure, and fluid density averaged over the pipe cross-section area, respectively; x stands for the spatial coordinate oriented along the axis of the pipe, t is the time, and τ_w is the wall shear stress. The one-dimensional assumption is justified by the fact that the aspect ratio of the considered pipe portion is equal to $l/d= 100$, where l stands for the length of the pipe-portion between the Flotec pressure sensor locations. Furthermore, the accuracy of the unidimensional approach has been proved in previous research where 3D model results have been compared for some Flotec applications [20, 21].

It is assumed, through the hypothesis of a local incompressible fluid for the piece of pipeline between the two pressure transducers, that $\frac{d\rho}{dt} \approx 0$. Hence, the liquid density variations due to the change in the mean pressure level are considered, while the density fluctuations due to the pressure oscillations around the time-averaged pressure level are neglected. The consistency of this hypothesis can be verified when the Mach number, defined as the ratio of the flow velocity to the speed of sound velocity, is lower than 0.1 [23]. Since the speed of sound under the isothermal assumption is higher than 1000 m/s for gasoline, diesel oil, and mineral oils, the abovementioned condition is satisfied for a large number of fluid power applications, if cavitation is not experienced. Therefore, the continuity equation reduces to $\frac{\partial u}{\partial x} = 0$, and the momentum balance equation becomes

$$
\frac{\partial u}{\partial t} + \frac{1}{\rho}\frac{\partial p}{\partial x} = -\frac{4\tau_w}{\rho d}
\tag{2}
$$

If Eq. 2 is multiplied by $\rho A/l$, where A represent the pipe cross-section area, by integrating over the distance l, one obtains:

132
$$\frac{d\overline{G}}{dt} = \frac{A}{l}\Delta p - \pi d \overline{\tau_w} \quad (3)$$

133 where G represents the mass flowrate and $\Delta p = p_{up} - p_{dw}$. The overlined quantities refer to the space-

134 averaged quantities along length l. By performing an integration of Eq. (3) with respect to time, one obtains

135 the space averaged flow-rate time history:

136
$$\bar{G}(t) = \overline{G_0} + \int_0^t \frac{A}{l} \Delta p \, dt - \pi d \int_0^t \overline{\tau_w} dt \quad (4)$$

137 where $\overline{G_0}$ represents the initial value of $\bar{G}(t)$, which is usually unknown. By conducting further analytical

138 steps, detailed in [19], it is possible to rewrite Eq. 4 as

139
$$\bar{G}(t) = \langle G \rangle + \frac{A}{l} \int_0^t [\Delta p - \langle \Delta p \rangle] \, dt - \pi d \Delta \overline{\Gamma}_{fdf} \quad (5)$$

140 where the angular brackets indicate time-averaged quantities and $\Delta \overline{\Gamma}_{fdf}$ is a function that depends on the

141 unsteady friction [19]. As can be inferred from Eq. (5), the instantaneous mass flowrate can be determined by

142 measuring the time-average flowrate $\langle G \rangle$ (e.g., by means of a Coriolis flowmeter) and the pressure difference,

143 Δp, along the considered pipe.

144   **4. Injector numerical model**

145 A 1D numerical model of the injector has been developed together with its feeding pipe and validated using

146 numerous experimental data for both single and pilot-main injections, over a range of nominal rail pressure

147 levels (p_{nom}) from 80 bar to 150 bar. This numerical diagnostic tool considers the main characteristics of the

148 high-pressure hydraulic circuit, the electromagnetic driving circuit and the mechanical components. Figure 4

149 shows a schematic of the injector numerical model. Generally, the circuit is constituted by 0D chambers linked

150 together by means of 1D pipes [24]. The Flotec pressure signal closest to the rail (p_{up}), as well as the current

151 (I) and the voltage (V) signals to the solenoid were selected as boundary conditions. By selecting this set of

152 boundary conditions, it was possible to avoid any inaccuracy in the modelling of the rail, the pump, and the

153 ECU [25]. The fluid is assumed as isothermal, and the energy equation therefore reduces to a state equation,

154 and the pipe model implements the generalized Euler partial differential equations, which are solved by means

155 of a Lax-Wendroff numerical method. The moving elements are governed by the ordinary differential form of

156　Newton's law, according to a mass-spring-damper approach. The forces involved in the numerical model can

157　be ascribed to hydraulic, mechanical, and electromagnetic phenomena. In particular, the electromagnetic force,

158　F_E, acting on the needle was evaluated as [1]:

159
$$F_E = -\frac{1}{2}\Phi^2 \frac{d\mathfrak{R}}{dx} \qquad (6)$$

160　where $\frac{d\mathfrak{R}}{dx}$ represents the variation in the circuit reluctance, namely $\mathfrak{R}$, with respect to the needle lift, and Φ is

161　the magnetic flux, which can be determined as:

162
$$\Phi = \frac{1}{S}\int_0^t [V(t) - RI(t)]dt \qquad (7)$$

163　Quantities V and I stand for the voltage and current that are applied to the injector solenoid, while R and S

164　represent the measured resistance and the number of solenoid windings, respectively. During the needle

165　movement, a viscous force is generated between the armature and the injector body, due to the presence of a

166　thin boundary layer. The flow in this small annular passage is laminar and follows Poiseuille's law. The viscous

167　friction force on the armature can therefore be evaluated as:

168
$$F_{vis} = \frac{\mu \cdot L_c \cdot v \cdot \pi \cdot d_a}{\delta_r} \qquad (8)$$

169　where d_a is the armature diameter, L_c is the length of the annular passage, δ_r is the radial distance between the

170　armature and the injector holder, μ is the flow dynamic viscosity, and v is the velocity of the needle.

171　The main geometrical features of the GDI injector, implemented in the numerical model, are reported in Table

172　1.

173
Table 1 - Main geometrical features of the tested injector.

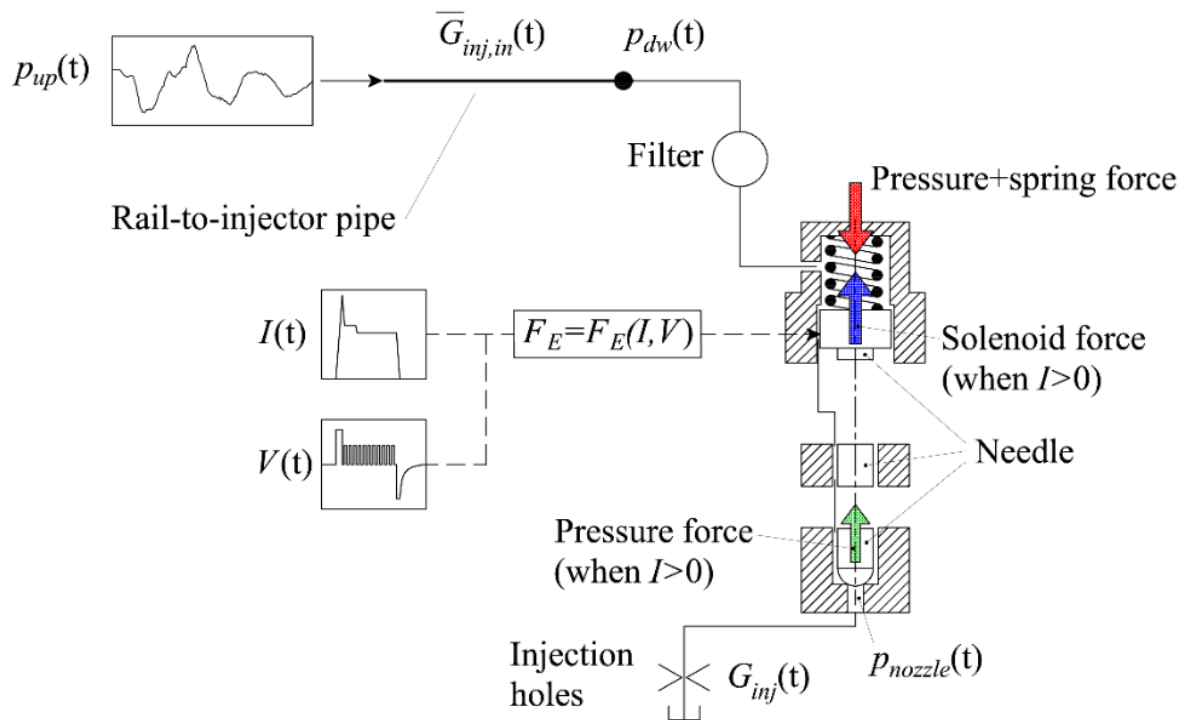| Property	Value
Number of holes [-]	6
Nozzle hole diameter [mm]	0.22
Needle length [mm]	30.9
Needle ball diameter [mm]	2.7
Armature diameter (d_a) [mm]	10
Annular passage length (L_c) [mm]	4.45
Armature radial distance (δ_r) [mm]	0.12

174

175

176

178

*Fig. 4 - Scheme of the numerical model of the GDI injector.*

179

180 The model validation involved a comparison of the numerical injected flowrate (G_{inj}) and of the numerical

181 pressure time history (p_{dw}) with the corresponding experimental traces, for both single and pilot-main

182 injections.

183 Furthermore, the numerical injector characteristic curves for different rail pressure levels over the previously

184 mentioned range were determined and compared with the experimental ones.

185 Figures 5 and 6 show the comparisons of the p_{dw} and G_{inj} time histories for a single and a pilot-main injection,

186 respectively: the symbols identify the experimental traces, while the lines refer to the numerical outcomes. As

187 can be inferred, the numerical results match the experimental ones perfectly, for both cases. This satisfactory

188 performance of the numerical model was verified over several $p_{nom} - ET$ working points for single injections,

189 and for several $p_{nom} - DT - ET_{main} - ET_{pil}$ sets for pilot-main injections.

190
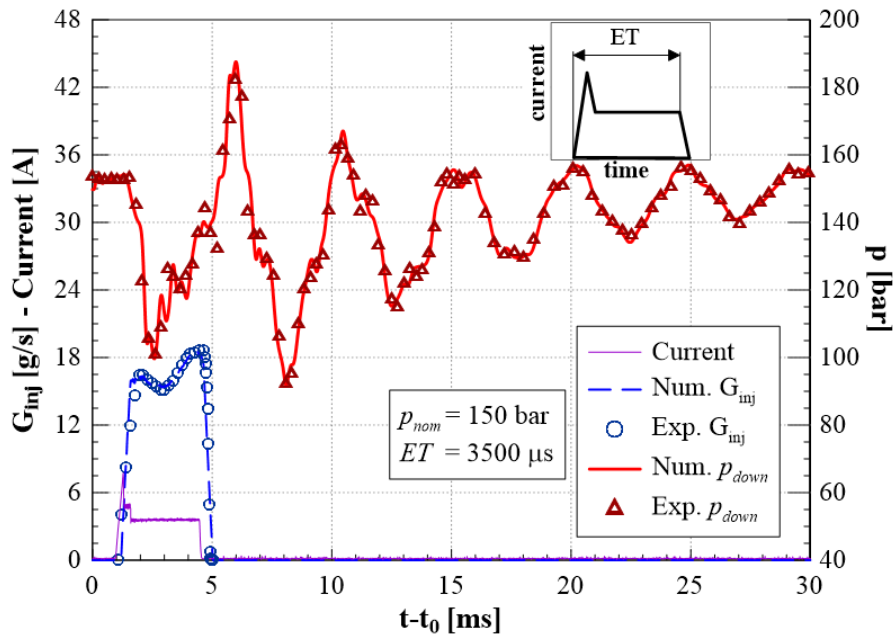
Fig. 5 - Comparison of the numerical and the experimental results for a single injection.

191
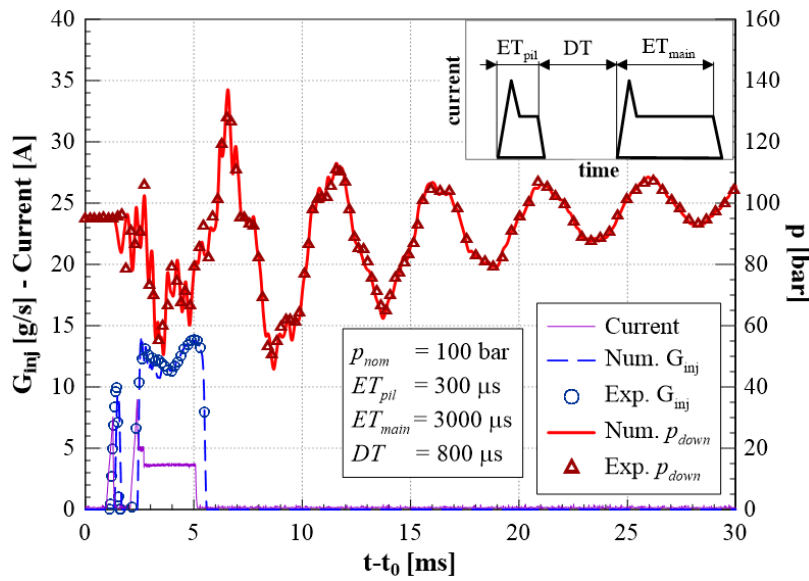
192

193

Fig. 6 - Comparison of the numerical and the experimental results for a pilot-main injection.

194

195   The comparison between the numerical and experimental injector characteristics is reported in Fig. 7 for

196   different p_{nom} levels (80 bar, 100 bar, 120 bar and 150 bar). The agreement between the numerical and the

197   experimental results is satisfactory, since the maximum error between the experimental injected mass and the

198   numerical one (such a difference includes the experimental inaccuracy) is less than 1.7 mg, a result that further
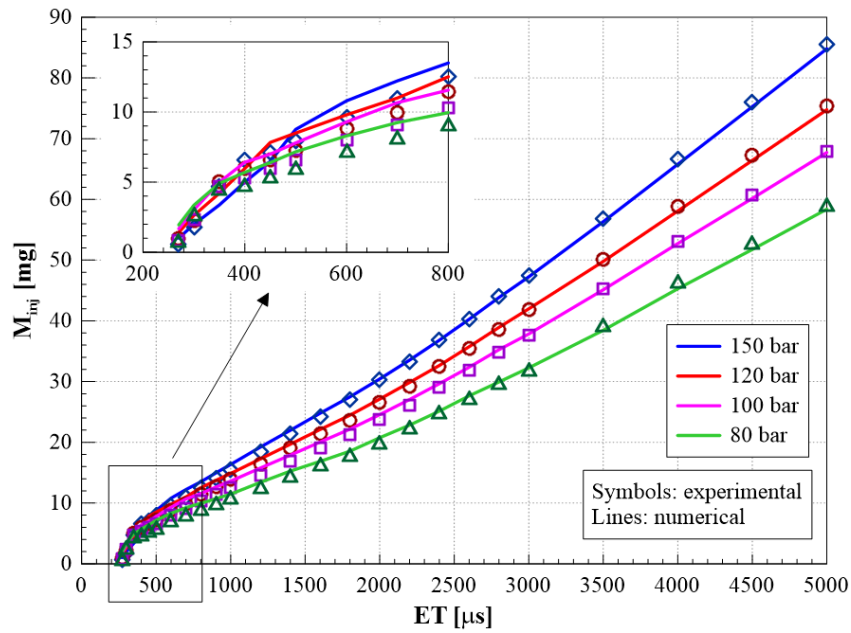
199   validates the model.

200

Fig. 7 – Numerical and experimental injector characteristics.

5. Experimental and numerical results

The numerical flowrate through the injector feeding pipe was determined from the 1D diagnostic tool (cf. Fig. 4). This numerical flowrate was compared with the experimental one measured with the flowmeter, and the results of this comparison are reported in Figs. 8 (single injection) and 9 (pilot-main injection): symbols are used to represent the numerical results and solid lines are utilized for the flowmeter data. As can be inferred from Figs. 8 and 9, the measured flowrates agree with those of the numerical diagnostic tool, and this further validates the new flowmeter. Since the compressibility of the flow is taken into account in the 1D numerical model, the good agreement shown in Figs. 8 and 9 demonstrates the consistency of the incompressible flow assumptions considered for the determination of the flowmeter.

From Fig. 7, it can be seen that the slope of the injector characteristic changes with respect to *ET*. The injected mass sharply increases with *ET* over the 270 μs ÷ 550 μs *ET* range. Figure 10 reports the normalized needle lifts (N/N_{max}) obtained using the numerical tool, the experimental injected flowrates, and the numerical pressure trace inside the nozzle (p_{nozzle}, cf. Fig. 4), for different *ET* values at p_{nom}= 150 bar. As can be seen in Fig. 10, when *ET*=350 μs or *ET*=450 μs, the injected flowrate is controlled by the needle seat area (the needle does not reach the end of its upper stroke over the considered *ET* range). When the needle reaches the end of its upper stroke (*ET*≈ 550 μs), the injected flowrate presents a local maximum and is controlled by the pressure drop
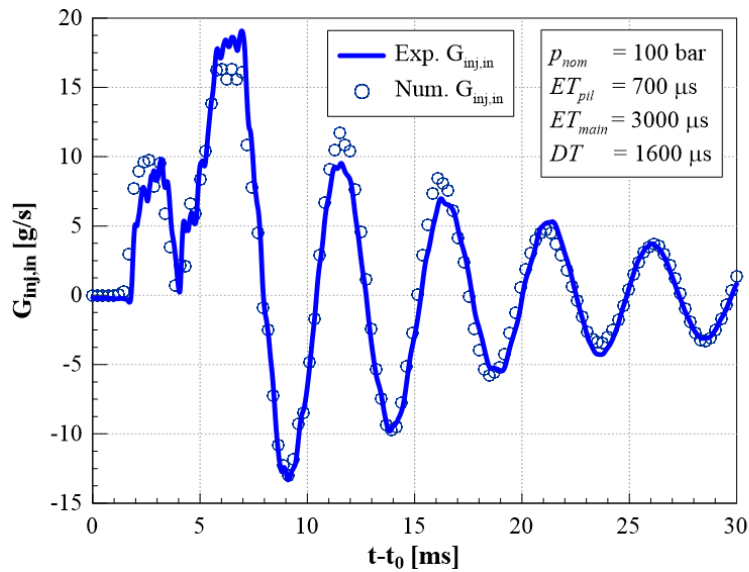
through the nozzle holes (cf. *ET*= 600 μs and *ET*= 1200 μs in Fig. 10). This explains the sharp augment in the injected mass over the 270 μs ÷ 550 μs *ET* range.
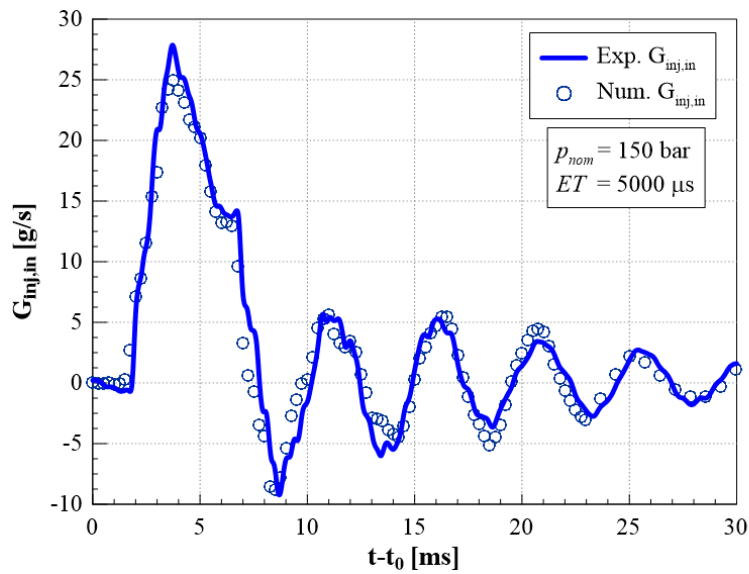
Fig. 8 - Comparison of the numerical and the measured injector-inlet flowrates for a single injection.

Fig. 9 - Comparison of the numerical and the measured injector-inlet flowrates for a pilot-main injection.

Furthermore, the *ET-M_{inj}* characteristic slope increases more when *ET*>2200 μs than over the *ET*= 550 μs ÷ 2200 μs range, for all the considered rail pressure levels (cf. Fig. 7). This phenomenon can be explained by considering the measured flowrate entering the injector and by analysing the propagation of the pressure waves throughout the high-pressure circuit of the fuel injection system [26].
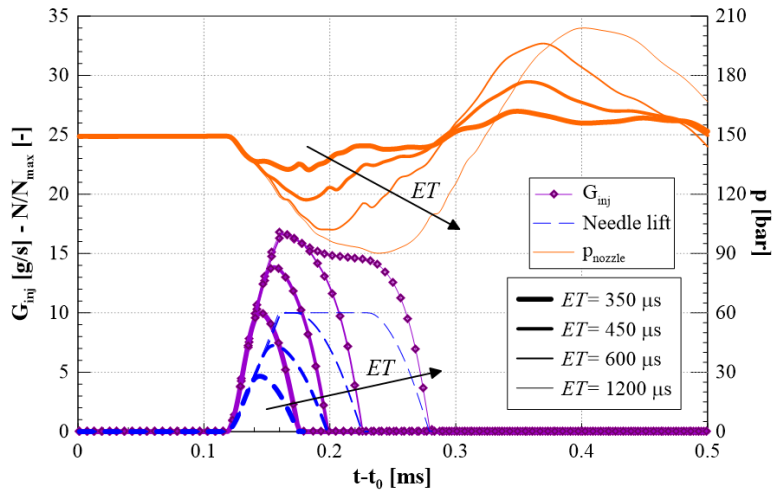
230

231

Fig. 10 - Needle lift, injected flowrate and nozzle pressure for different ETs.
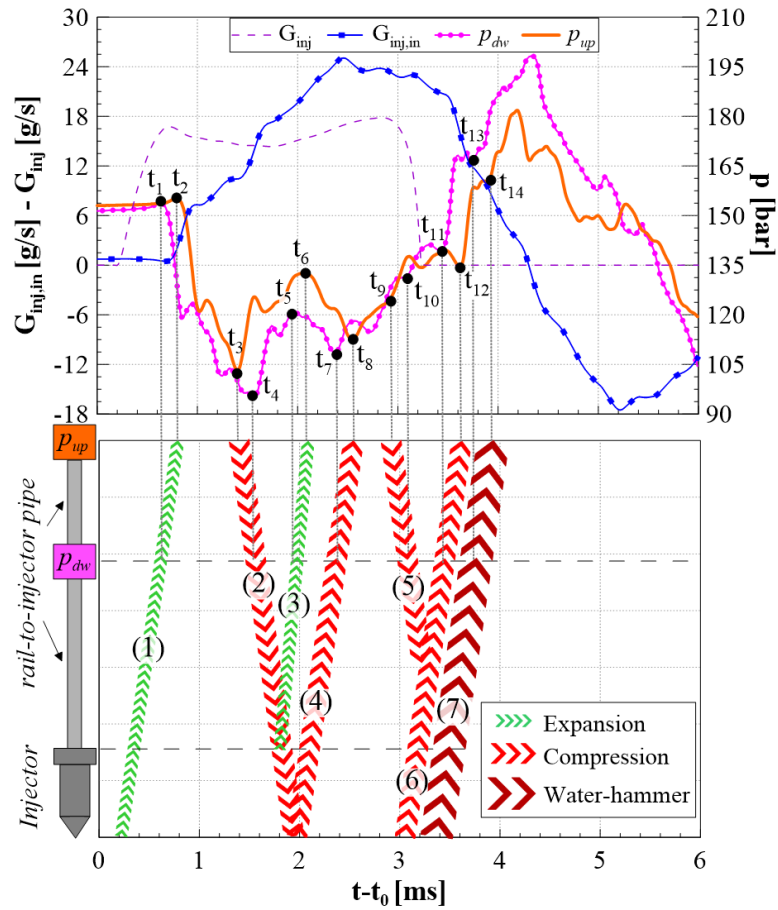
232

233

Fig. 11 – Propagation of the pressure waves in the hydraulic circuit (p_{nom} = 150 bar, ET = 2800 μs).

234   The upper part of Fig. 11 reports the measured flowrate at the injector inlet, the p_{up} and p_{dw} pressure signals,

235   and the measured injected flowrate for an injection schedule of p_{nom}= 150 bar and *ET*= 2800 μs, while a

236   schematic representation of the propagation of the pressure waves through the hydraulic circuit is presented in

237   the lower part, where the circuit is represented in scale on the left of the bottom graph and the vertical axis

238 reports a spatial coordinate. When the needle opens the nozzle and the injected flowrate start to rise, an

239 expansion wave (1), which is the first wave experienced by the hydraulic system, travels from the injector to

240 the rail and, consequently, a pressure drop can be observed in p_{dw} (at $t=t_1$) and, after a certain delay, in p_{up} (at

241 $t=t_2$). Thus, from these time instants, the first expansion wave travelling from the injector tip to the rail can be

242 represented, as shown in the bottom graph of Fig. 11, between the spatial locations referring to p_{up} and p_{dw}.

243 When this wave reaches the rail, it is reflected as a compression wave (2); the pressure rise in p_{up} ($t=t_3$) occurs

244 in advance, with respect to that in p_{dw} ($t=t_4$), and this indicates that the pressure wave is travelling from the rail

245 toward the injector. Such a compression can be extended up to the nozzle. Another reflection occurs in this

246 hydraulic circuit when a wave reflected by the rail enters the injector, due to the difference in the diameter

247 between the injector feeding pipe and the injector entrance. The presence of a pressure drop that first occurs

248 in p_{dw} ($t=t_5$) and then in p_{up} ($t=t_6$) justifies the presence of a partial reflection, as an expansion wave (3) of the

249 compression wave (2) that is entering the injector. Wave (3) can be represented in the graph when the t_5 and t_6

250 time instants are known. When the compression wave (2) reaches the injector tip, it is reflected as a

251 compression wave (4), which travels toward the rail, as the occurrence of the pressure rise first in p_{dw} ($t=t_7$)

252 and then in p_{up} ($t=t_8$) confirms. In the meanwhile, the expansion wave (3) has reached the rail and has been

253 reflected as a compression wave (5) that travels toward the injector, thus implying a further pressure rise in p_{up}

254 ($t=t_9$) and then in p_{dw} ($t=t_{10}$). Prior to the reflection of this wave (5) at the injector entrance, the injected flowrate

255 decreases as the needle starts its downward stroke and, when the entering flowrate exceeds the injected one, a

256 compression wave (6) leaves the needle seat area and propagates upstream, thus leading to a pressure rise that

257 is detected first in p_{dw} ($t=t_{11}$) and then in p_{up} ($t=t_{12}$). In a similar way to the first expansion wave (1), by

258 identifying the time instants t_{11} and t_{12}, which refer to a compression wave moving from p_{dw} to p_{up}, and by

259 extending this wave backward till it reaches the injector tip, it can be confirmed that it starts during the

260 descending phase of G_{inj}, i.e., when the needle is moving downward. Finally, as the needle reaches the end of

261 its downstroke (the injected flowrate is null), a water-hammer (7) is triggered in the nozzle and this drives an

262 impulsive pressure rise in p_{dw} ($t=t_{13}$) and then in p_{up} ($t=t_{14}$). For conciseness reasons, the expansion wave given

263 by the reflection of the compression wave (4) in the rail has been omitted from the figure (the time instants at

264 which p_{up} and, subsequently, p_{dw} start to decrease can easily be identified between t_{10} and t_{11}). It can be noted,

265 from the pressure waves propagation motion schematized in Fig. 11, that, at the beginning of the injection, the

266   fuel in the rail-to-injector pipe is accelerated toward the injector nozzle, due to the presence of the

267   expansion wave (1); the compression wave (2) then pushes the flow toward the nozzle, and, finally, even the

268   expansion wave (3) tends to accelerate the injected fuel. Instead, the compression wave (4) opposes the fuel

269   going toward the injector and, as a result, the measured flowrate features a maximum. For $ET \geq 2200$ μs (cf.

270   Fig. 11), compression waves (2) and (5) help to push a flowrate into the injector, making the nozzle pressure

271   rise monotonically with respect to the time and, consequently, the increased injected flowrate makes the slope

272   of the ET-M_{inj} injector characteristics augment (cf. Fig. 7). $ET= 2200$ μs is the first value at which the

273   compression wave (2) has almost recovered the initial pressure drop, induced by the start of the injection,

274   within the nozzle.

275   As already presented in the literature [27]–[29], the mass entering the injector can be used to set up a closed-

276   loop strategy of the injected mass. If the flowrate time history that enters the injector is integrated till it reaches

277   its absolute minimum (cf. Fig. 8 at t=8.5 ms), a robust correlation between the injected fuel quantity (M_{inj}) and

278   the mass that enters the injector during an injection event ($M_{inj,in}$) can be obtained; such a correlation is reported

279   as a continuous line in Fig. 12, where the experimental points are plotted with symbols. In [27]–[29], the mass

280   entering the diesel Common Rail injector, $M_{inj,in}$, was obtained by ending the integration of the injector inlet

281   flowrate in correspondence to its absolute maximum value. This difference in the method can be ascribed to

282   the fact that, since the GDI injector pressure working range is much smaller than that of a diesel Common Rail

283   injector, the energizing times are generally much longer. Therefore, if one wants to select the absolute

284   maximum of the flowrate to terminate the integration of large ETs, the fuel injection would still be underway

285   at that time, and the obtained entering mass would not be fully representative of the injected one.

286   The scheme of a possible closed-loop control is represented in Fig. 13. During an injection event, p_{up} and p_{dw}

287   are measured by means of the Flotec flowmeter pressure sensors, which provide the flowrate that enters the

288   injector, namely $G_{inj,in}$ (cf. the red box in Fig. 13). The mass that enters the injector can be obtained by

289   integrating $G_{inj,in}$ with respect to time. This mass is used as input to obtain a prediction of the injected mass (cf.

290   the green box in Fig. 13), on the basis of the previously-determined correlation $M_{inj,pred}=f(M_{inj,in})$ represented

291   in Fig. 12. The $M_{inj,pred}$, value is then compared with the target value of the injected fuel quantity, i.e $M_{inj,ref}$,

292   (this datum is stored in the ECU), and the $\Delta M_{inj}= M_{inj,ref} -M_{inj,pred}$ difference is generated (cf. the blue box in

293   Fig. 13). Such an estimation of the error in the injected mass is used as an input datum of a PID controller,

Such a control can be used, for example, to correct the injected mass inaccuracy for a fixed couple of nominal

rail pressure level and energizing times, when the injector nozzle holes are affected by coking deposits [30],

[31].
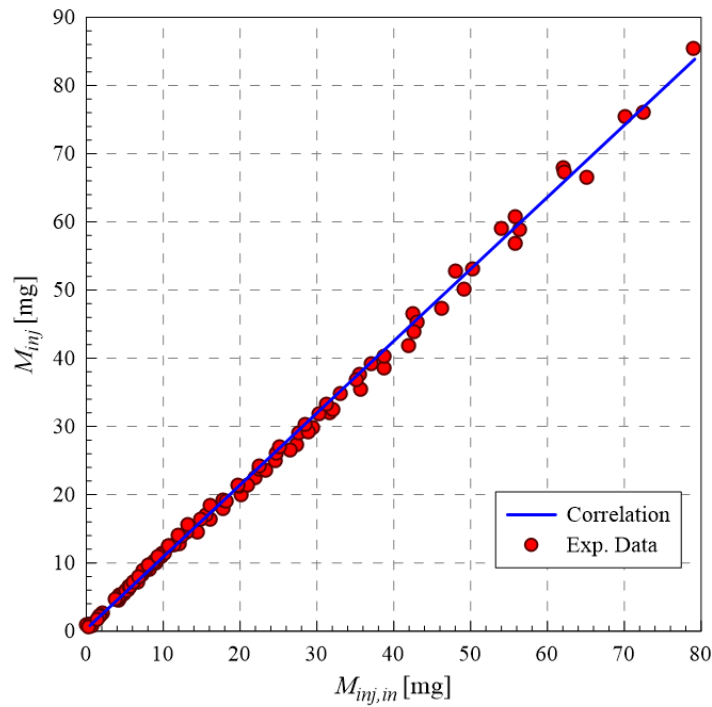
Fig. 12- Correlation between the mass at the injector entrance and the injected one.

: Measurement of the mass entering the injector ($M_{inj,in}$);

: Prediction of the injected mass ($M_{inj,pred}$);

: Calculation of the *ET* correction ($ΔET$) on the basis of the injected mass inaccuracy ($ΔM_{inj}$);
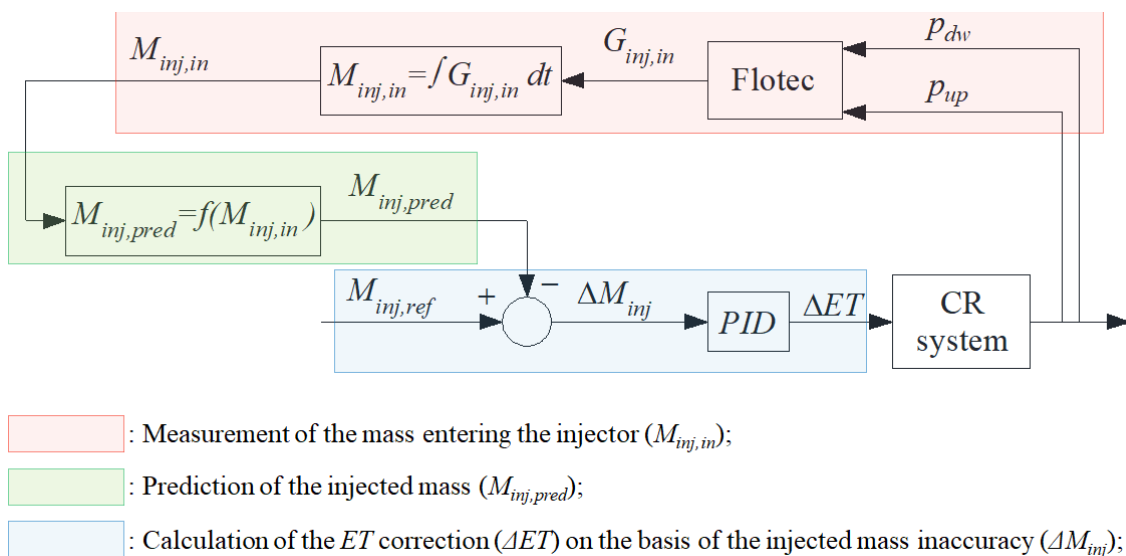
Fig. 13 - Scheme of the closed-loop control for the injected mass.

6. Conclusions

The high-pressure, instantaneous, liquid flowrate along a pipeline has been measured by employing an innovative flowmeter. This flowrate was obtained from two pressure signals, p_{up} and p_{dw}, measured at a distance of 200 mm from each other, along the investigated pipe. The flowmeter algorithm combines the momentum balance and the mass conservation equations for a 1D locally incompressible flow. The flowmeter was employed to measure the flowrate that enters a GDI injector during operation. The injector was fed through an 840 mm long pipe that had been equipped with the innovative flowmeter. A 1D numerical tool of the injector plus its feeding line was realized to further assess the consistency of the measured flowrate that entered the injector. This model receives the p_{up} pressure signal (used for the flowrate measurement) as a boundary condition and the current and voltage to the injector solenoid as input signals. The model was then validated successfully by means of comparisons between the numerical pressure time history at the location of the second pressure transducer (p_{dw}) and the corresponding experimental trace, and by comparing the numerical injected flowrate and the experimental trace, measured by means of a Bosch method-based low-pressure flowmeter. Both single and pilot-main injections were considered, and the numerical outcomes accurately matched the experimental traces for different working conditions. The ET-M_{inj} injector characteristics showed two changes in slope. It has been shown, using the numerical model, that the needle does not reach the end of its upstroke over the first ET range (ET<550 μs), and this leads to a sharp increase in M_{inj} with ET. When ET> 550 μs, the flowrate starts to be controlled by the pressure drop across the nozzle holes, and the slope of the curve reduces. An increment in the characteristic slope can be observed when ET≥2200 μs. It has been shown that, at the beginning of the injection, the flowrate is accelerated toward the nozzle by an expansion wave that arises in the nozzle, and that it is finally pushed toward the injector by a compression wave that comes from the rail. When ET≥2200 μs, the nozzle pressure rises monotonically, due to a further flowrate that is pushed inside the injector by two other compression waves. This pressure rise leads to an increased injected flowrate that makes the slope of the injector characteristics augment. The flowrate that enters the injector can be integrated by selecting two arbitrary time instants to obtain a mass. In this case, the integration was performed from the start of the electric command up to the absolute minimum experienced by the measured injector-inlet flowrate. This entering mass can be correlated to the outlet mass to set up a closed-loop control that can be employed to modulate the ET during online injector operation. In fact, by means of the feedback signal of the mass that

enters the injector, a prediction of the effective injected fuel quantity can be determined on the basis of the previously determined correlation. Thus, by comparing the mass prediction with the target value stored in the ECU, the injected mass inaccuracy due, for example, to the presence of coking deposits on the nozzle holes or to thermal drifts, can be corrected.

Acknowledgments

Nomenclature

0D	zero-dimensional
1D	one-dimensional
3D	three-dimensional
A	pipe cross-section area
d	diameter, pipe diameter
DT	dwell time
ET	energizing time
F	force
FMV	fuel metering valve
G	mass flowrate
I	current signal
IA	injection analyzed
L_c	length of the annular passage
l	distance between the Flotec pressure sensors
M	mass
N	needle lift
p	flow pressure
PCV	pressure control valve
R	resistance
$\Re$	reluctance
S	number of solenoid windings
t	time

361   u flow velocity

362   V voltage signal

363   v needle velocity

364   x spatial coordinate

365   ΔET energizing time correction

366   ΔM_{inj} difference between the reference injected mass and the predicted one

367   $\Delta \bar{\Gamma}_{fdf}$ unsteady friction function

368   Δp pressure difference along the Flotec pipe

369   δ_r radial distance between the armature and the injector holder

370   Φ magnetic flux

371   μ flow dynamic viscosity

372   ρ flow density

373   τ_w wall shear stress

374   ***Subscritps***

375   0 initial value

376   a armature

377   dw referring to the Flotec pressure sensor close to the injector

378   E electromagnetic

379   inj injected

380   inj,in entering the injector

381   $main$ main injection

382   max maximum

383   nom nominal

384   $nozzle$ referring to injector nozzle

385   pil pilot injection

386   $pred$ prediction

387   ref reference

388   up referring to the Flotec pressure sensor close to the rail

389   vis viscous friction

390   **References**

391   [1]   A. E. Catania, A. Ferrari, and M. Manno, "Development and Application of a Complete Multijet
392   Common-Rail Injection-System Mathematical Model for Hydrodynamic Analysis and Diagnostics," *J
393   Eng Gas Turbine Power*, vol. 130, no. 6, Nov. 2008, doi: 10.1115/1.2925679.

394   [2]   I. De Souza *et al.*, "Calibration of a Cryogenic Turbine-Based Volumetric Flow Meter (CTVFM)
395   Using Sub-Cooled Liquid Nitrogen and Solution for Its Practical Issues," *IEEE Sens J*, vol. 21, no.
396   10, pp. 12077–12083, May 2021, doi: 10.1109/JSEN.2021.3065309.

397   [3]   I. Gaskin, E. Shapiro, and D. Drikakis, "Theoretical, Numerical, and Experimental Study of the Time
398   of Flight Flowmeter," *J Fluids Eng*, vol. 133, no. 4, Apr. 2011, doi: 10.1115/1.4003852.

399   [4]   R. Cheesewright, K. N. Atkinson, C. Clark, G. J. P. ter Horst, R. C. Mottram, and J. Viljeer, "Field
400   tests of correction procedures for turbine flowmeters in pu satile flows," *Flow Measurement and
401   Instrumentation*, vol. 7, no. 1, pp. 7–17, Mar. 1996, doi: 10.1016/0955-5986(96)00004-0.

402   [5]   B. Lee, R. Cheesewright, and C. Clark, "The dynamic response of small turbine flowmeters in liquid
403   flows," *Flow Measurement and Instrumentation*, vol. 15, no. 5–6, pp. 239–248, Oct. 2004, doi:
404   10.1016/j.flowmeasinst.2004.07.002.

405   [6]   Z. Džemić, B. Širok, and B. Bizjan, "Turbine flowmeter response to transitional flow regimes," *Flow
406   Measurement and Instrumentation*, vol. 59, pp. 18–22, Mar. 2018, doi:
407   10.1016/j.flowmeasinst.2017.11.006.

408   [7]   J. Dong, C. Jing, Y. Peng, Y. Liu, H. Ren, and X. Liu, "Study on the measurement accuracy of an
409   improved cemented carbide orifice flowmeter in natural gas pipeline," *Flow Measurement and
410   Instrumentation*, vol. 59, pp. 52–62, Mar. 2018, doi: 10.1016/j.flowmeasinst.2017.12.008.

411   [8]   A. Raheem, A. S. B. Siddiqi, A. Ibrahim, A. Ullah, and M. H. Inayat, "Evaluation of multi-holed
412   orifice flowmeters under developing flow conditions – An experimental study," *Flow Measurement
413   and Instrumentation*, vol. 79, p. 101894, Jun. 2021, doi: 10.1016/j.flowmeasinst.2021.101894.

414   [9]   M. Moosa and M. H. Hekmat, "Numerical investigation of turbulence characteristics and upstream
415   disturbance of flow through standard and multi-hole orifice flowmeters," *Flow Measurement and
416   Instrumentation*, vol. 65, pp. 203–218, Mar. 2019, doi: 10.1016/j.flowmeasinst.2019.01.002.

417   [10] V. P. Head, "Discussion: 'Small-Diameter-Orifice Metering' (Filban, T. J., and Griffin, W. A., 1960,
418   ASME J. Basic Eng., 82, pp. 735–738)," *Journal of Basic Engineering*, vol. 82, no. 3, pp. 739–739,
419   Sep. 1960, doi: 10.1115/1.3662732.

420   [11] E. O. Doebelin and D. N. Manik, *Measurement systems: application and design*. McGraw-Hill, 2007.
421   Accessed: Mar. 27, 2023. [Online]. Available:
422   https://inis.iaea.org/search/search.aspx?orig_q=RN:42014391

423   [12] T. Wang and R. Baker, "Coriolis flowmeters: a review of developments over the past 20 years, and an
424   assessment of the state of the art and likely future directions," *Flow Measurement and
425   Instrumentation*, vol. 40, pp. 99–123, Dec. 2014, doi: 10.1016/J.FLOWMEASINST.2014.08.015.

426   [13] J. Zhao, L. Grekhov, and P. Yue, "Limit of Fuel Injection Rate in the Common Rail System under
427   Ultra-High Pressures," *International Journal of Automotive Technology*, vol. 21, no. 3, pp. 649–656,
428   Jun. 2020, doi: 10.1007/s12239-020-0062-3.

429   [14] X. Li *et al.*, "Comparative Study on the Macroscopic Characteristics of Gasoline and Ethanol Spray
430   from a GDI Injector under Injection Pressures of 10 and 60 MPa," *ACS Omega*, vol. 7, no. 10, pp.
431   8864–8873, Mar. 2022, doi: 10.1021/acsomega.1c07188.

432   [15] S. Gul, J. Shiriyev, V. Singhal, O. Erge, and C. Temizel, "Advanced materials and sensors in well
433   logging, drilling, and completion operations," in *Sustainable Materials for Oil and Gas Applications*,
434   Elsevier, 2021, pp. 93–123. doi: 10.1016/B978-0-12-824380-0.00004-9.

435   [16] Kulite, *Innovative Piezoresistive Transducers*. 2007.

[17] A. Ferrari and T. Zhang, "Benchmark between Bosch and Zeuch method–based flowmeters for the measurement of the fuel injection rate," *International Journal of Engine Research*, vol. 22, no. 1, pp. 316–327, Jan. 2021, doi: 10.1177/1468087419827732.

[18] A. Ferrari, Z. Jin, O. Vento, and T. Zhang, "An injected quantity estimation technique based on time–frequency analysis," *Control Eng Pract*, vol. 116, p. 104910, Nov. 2021, doi: 10.1016/j.conengprac.2021.104910.

[19] A. Ferrari and P. Pizzo, "Optimization of an Algorithm for the Measurement of Unsteady Flow-Rates in High-Pressure Pipelines and Application of a Newly Designed Flowmeter to Volumetric Pump Analysis," *J Eng Gas Turbine Power*, vol. 138, no. 3, Mar. 2016, doi: 10.1115/1.4031541.

[20] A. Corvaglia, A. Ferrari, M. Rundo, and O. Vento, "Three-dimensional model of an external gear pump with an experimental evaluation of the flow ripple," *Proc Inst Mech Eng C J Mech Eng Sci*, vol. 235, no. 6, 2021, doi: 10.1177/0954406220937043.

[21] A. Ferrari, P. Fresia, M. Rundo, O. Vento, and P. Pizzo, "Experimental Measurement and Numerical Validation of the Flow Ripple in Internal Gear Pumps," *Energies (Basel)*, vol. 15, no. 24, 2022, doi: 10.3390/en15249607.

[22] A. Ferrari and O. Vento, "Influence of Frequency-Dependent Friction Modeling on the Simulation of Transient Flows in High-Pressure Flow Pipelines," *Journal of Fluids Engineering, Transactions of the ASME*, vol. 142, no. 8, 2020, doi: 10.1115/1.4046623.

[23] G. K. Batchelor, *An Introduction to Fluid Dynamics*. Cambridge University Press, 2000. doi: 10.1017/CBO9780511800955.

[24] Z. Jin *et al.*, "Numerical-experimental optimization of the common-feeding injection system concept for application to light-duty commercial vehicles," *Journal of Energy Resources Technology, Transactions of the ASME*, vol. 143, no. 12, 2021, doi: 10.1115/1.4050133.

[25] A. Ferrari and O. Vento, "Thermal effects on Common Rail injection system hydraulic performance," *International Journal of Engine Research*, p. 146808742311624, Mar. 2023, doi: 10.1177/14680874231162412.

[26] M. Baratta, A. E. Catania, and A. Ferrari, "Hydraulic Circuit Design Keys to Remove the Dependence of the Injected Fuel Amount on Dwell Time in Multi-Jet C.R. Systems," in *ASME 2006 Internal Combustion Engine Division Spring Technical Conference (ICES2006)*, ASMEDC, Jan. 2006, pp. 465–477. doi: 10.1115/ICES2006-1426.

[27] A. Ferrari, C. Novara, E. Paolucci, O. Vento, M. Violante, and T. Zhang, "Design and rapid prototyping of a closed-loop control strategy of the injected mass for the reduction of CO_2, combustion noise and pollutant emissions in diesel engines," *Appl Energy*, vol. 232, 2018, doi: 10.1016/j.apenergy.2018.09.028.

[28] A. Ferrari, C. Novara, E. Paolucci, O. Vento, M. Violante, and T. Zhang, "A new closed-loop control of the injected mass for a full exploitation of digital and continuous injection-rate shaping," *Energy Convers Manag*, vol. 177, 2018, doi: 10.1016/j.enconman.2018.08.037.

[29] A. Ferrari, C. Novara, O. Vento, M. Violante, and T. Zhang, "A novel fuel injected mass feedback-control for single and multiple injections in direct injection systems for CI engines," *Fuel*, vol. 334, 2023, doi: 10.1016/j.fuel.2022.126670.

[30] F. Pickl, M. Russer, M. Hauenstein, and M. Wensing, "Modelling and understanding deposit formation and reduction in combustion engines – Application to the concrete case of internal GDI injector deposit," *Fuel*, vol. 236, pp. 284–296, Jan. 2019, doi: 10.1016/J.FUEL.2018.08.139.

479   [31]   J. B. J. Reid *et al.*, "The Investigation of the Structure and Origins of Gasoline Direct Injection (GDI)
480   Deposits.," Dec. 2019. doi: 10.4271/2019-01-2356.

481